Detection and Measurement of Gas Concentration Using Infrared Single Pixel Camera

Sebastian Urbaś, Robert Olbrycht, Bogusław Więcek
Lodz University of Technology, Institute of Electronics, Al. Politechniki 6, Lodz, 90-924, Poland
Krzysztof Szajewski
Military University of Technology, Faculty of Cybernetics, gen. Sylwestra Kaliskiego 2 Street, 00-908, Warsaw, Poland
Anna Szajewska
Fire University, Faculty of Safety Engineering and Civil Protection, 52/54 Słowackiego Street, Warsaw, 01-629, Poland

Abstract: This paper presents an innovative method for detecting and quantifying carbon dioxide CO_2 using a Single Pixel Camera (SPC) operating in the Mid-Wave Infrared (MWIR) spectral range. Instead of a conventional detector array, the system employs a single HgCdTe photodetector coupled with a rotating Spatial Light Modulator (SLM) encoded with cyclic Hadamard masks. Image reconstruction is performed mathematically based on sequential measurements which enable both image quality improvement and interpolation with a reduced number of samples. The developed system allows for the generation of two-dimensional images of infrared radiation distribution attenuated by the presence of CO_2, enabling remote estimation of its concentration. Laboratory experiments were conducted using a controlled gas chamber and a reference photoacoustic sensor. The results confirm the system's capability to accurately measure CO_2 concentrations in the range 1,000–32,500 ppm, with an expanded uncertainty not exceeding 6 %. The proposed technology combines low detector cost with high sensitivity and spatial imaging capabilities. It shows promising potential for applications in environmental monitoring, gas leak detection, and compact systems for atmospheric and air quality analysis.

Keywordse: single pixel IR camera, CO_2 MWIR absorption, Hadamard cyclic matrix

1. Introduction

Currently, there are numerous methods for detecting and quantifying CO_2 in the atmosphere. Techniques such as chromatographic analysis [1, 2], gravimetric analysis [3], or electrochemical sensor measurements [4] enable precise determination of CO_2 concentration; however, these measurements must be performed directly on collected samples. A significantly more convenient approach is the use of optical measurement methods, which rely on the transmission or absorption of electromagnetic waves. Both of these phenomena, which facilitate the determination of CO_2 concentration, are related to the specific properties of CO_2 in absorbing radiation energy at characteristic wavelengths. The absorption of radiation at specific wavelengths by CO_2 results from the matching of the energy of incident photons to the energy gaps between allowed quantized energy levels [5, 6]. The CO_2 molecule is linear. For a linear molecule consisting of n atoms, the number of possible vibrational modes is given by $3n - 5$ [7]. For CO_2 (three atoms), there are four independent normal vibrational modes, which include:

1. Symmetric stretching vibration – oxygen atoms move in opposite directions relative to the carbon atom, causing the bond lengths to change symmetrically;
2. Asymmetric stretching vibration – one oxygen atom moves away from the carbon atom while the other moves closer, maintaining a constant total length of the two oxygen atoms constant;
3. In-plane bending vibration – The molecule "bends" within the plane of the bonds;
4. Out-of-plane bending vibration – The molecule "bends" outside the plane of the bonds.

Each type of vibration requires a specific amount of energy corresponding to its resonant frequency, which is necessary to induce a change in the energy level [8]. In the case of CO_2, the bending vibrations share the same energy level. Consequently, there are three fundamental vibrational energy levels, corresponding to the following wavelengths: v_1 – 7.5 μm, v_2 – 15 μm, and v_3 – 4.3 μm. Radiation absorption occurs only when the dipole moment of the molecule changes, altering the distribu-

Autor korespondujący:
Sebastian Urbaś, sebastian.urbas@dokt.p.lodz.pl

Artykuł recenzowany
nadesłany 18.05.2026 r., przyjęty do druku 27.07.2026 r.

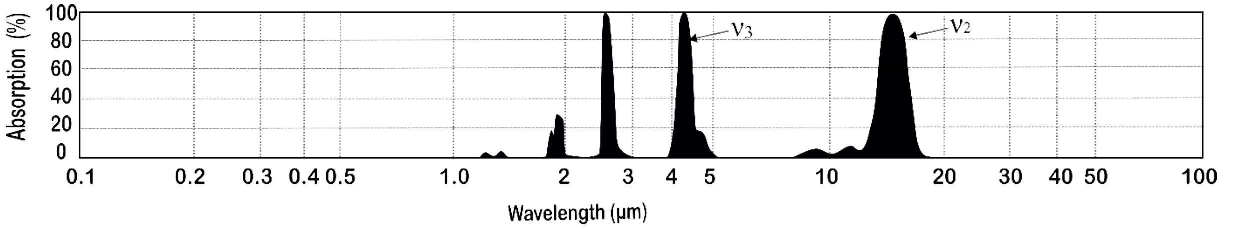

Fig. 1. Infrared absorption spectrum of CO_2. The labels ν_2 and ν_3 denote the bending and asymmetric stretching vibrational modes, respectively. The remaining absorption bands arise from overtones and combination bands. Developed by the authors based on spectroscopic data from the HITRANonline database

Rys. 1. Widmo absorpcji CO_2 w zakresie podczerwieni. Oznaczenia ν_2 i ν_3 odpowiadają odpowiednio drganiom zginającym i asymetrycznym drganiom rozciągającym cząsteczki. Opracowanie własne na podstawie danych z bazy HITRANonline [https://hitran.org]

tion of charge within it [9]. In the case of CO_2, the symmetric stretching vibration (v_1) does not induce a dipole moment change, meaning that no infrared (IR) absorption occurs at this frequency. Beyond the fundamental vibrational frequencies, CO_2 also exhibits harmonic frequencies (overtones) and combination bands (sum and difference bands) [10, 11]. Additionally, these wavelengths may experience slight shifts due to the spin energy of the molecule, causing the spectral lines to appear broadened rather than perfectly sharp. As a result, CO_2 exhibits a unique absorption spectrum, as illustrated in Fig. 1. Several distinct absorption bands are visible, with strong absorption near 4.3 μm and 15 μm, corresponding to asymmetric stretching (v_3) and bending vibrations (v_2), respectively. The remaining peaks arise from a combination of fundamental frequencies, overtones, and combination bands.

There are various optical methods for detecting CO_2 [12]. In the absorption-based method, a beam of radiation passes through the analyzed gas, and the molecules within it absorb specific wavelengths of the radiation. The oldest measurement method used for CO_2 detection is Non-Dispersive InfraRed (NDIR) spectroscopy [13]. In this technique, an infrared (IR) radiation source emits broadband IR radiation that includes wavelengths absorbed by CO_2. An optical filter allows only a specific wavelength corresponding to the CO_2 absorption band (4.26 μm) to pass through, effectively eliminating other wavelengths and minimizing interference from other gases. The determination of CO_2 concentration is based on measuring the attenuation of the transmitted signal relative to the reference signal (without the sample), following Beer-Lambert's law. NDIR-based devices are characterized by high durability and resistance to environmental factors. Furthermore, in this method, the radiation source can be placed at a significant distance from the detector, making it suitable for remote sensing applications. NDIR technology is also utilized in space research and extraterrestrial atmospheric analysis [14].

An alternative method to NDIR is Tunable Diode Laser Absorption Spectroscopy (TDLAS), which utilizes a tunable diode laser with an adjustable wavelength [15, 16]. Unlike NDIR, which relies on selective filtering of a specific wavelength, TDLAS illuminates the sample with laser light whose wavelength is continuously tuned. The laser beam is transmitted through a sample containing the target gas. By precisely tuning the wavelength to match one of the absorption lines of the gas and measuring the absorption intensity, it is possible to accurately determine the gas concentration.

Another approach is Differential Optical Absorption Spectroscopy (DOAS) [17]. This technique utilizes a high-intensity xenon lamp, which generates a light beam that is projected through an open space to a receiver. An alternative setup involves placing the receiver next to the lamp, with the radiation being reflected from a mirror positioned on the opposite side. The optical path length can reach up to 1 km. By analyzing the absorption of a broad UV-VIS radiation spectrum by CO_2, a spectrophotometer placed in the receiver can determine the gas concentration based on differential absorption measurements. The key advantages of this method include long-range detection and the ability to simultaneously measure multiple gases. However, absorption in the visible (VIS) and near-infrared (NIR) ranges is relatively weak, limiting the accuracy of the method for CO_2 detection. Additionally, atmospheric conditions significantly affect measurement accuracy, making the technique sensitive to external environmental factors.

The amount of absorbed radiation can be determined using the Photoacoustic Spectroscopy (PAS) method [18, 19]. The absorption intensity depends on the CO_2 concentration in the sample, which enables both its identification and quantification [20]. This method is based on the conversion of electromagnetic radiation energy into acoustic waves within the analyzed gas sample. When the sample is exposed to modulated radiation of a specific wavelength, the absorbed energy is converted into heat as the excited molecules relax back to their ground state. Since the radiation is modulated at a specific frequency, the cyclic heating and cooling of the gas generates an acoustic wave at the same frequency as the modulation of the incident radiation. The CO_2 concentration is determined by measuring the amplitude of the acoustic wave, using detectors such as piezoelectric microphones [21]. PAS-based detectors are compact and highly sensitive, but they have a limited operational range.

Another method for determining CO_2 concentration is Cavity Ring-Down Spectroscopy (CRDS). This technique is based on measuring the decay time of laser radiation after multiple reflections within an optical measurement cavity. The higher the number of CO_2 absorbing molecules in the cavity, the faster the light is absorbed, resulting in a shorter decay time [22]. CRDS is a fast and highly sensitive technique that is independent of the power of the light source. However, its accuracy depends on the optical path length, environmental conditions, vibrations, and calibration precision. The operational range is limited by the size of the measurement chamber.

As an alternative to point-based measurement methods, 2D and 3D CO_2 imaging can be performed using Hyper-spectral Light Detection and Ranging (LiDAR) [23]. In this technique, a laser emits a beam at a specific wavelength in a chosen direction. The laser beam is partially absorbed by atmospheric CO_2 or reflected from the Earth's surface, and the returning light carries information about the CO_2 concentration. The measurement can be performed using Differential Absorption LiDAR (DIAL) [24], which relies on differential absorption at two wavelengths, or through spectrophotometric analysis, which determines CO_2 concentration based on spectral characteristics [25]. By analyzing the time of the returning laser beam, CO_2 concentration can be mapped at different altitudes, enabling atmospheric profiling and spatial visualization of CO_2 distribution.

Single-pixel cameras (SPCs) represent a compelling alternative to conventional imaging systems that rely on array detectors, particularly within the mid-wave IR (MWIR) and long-wave IR (LWIR) spectral regions. Rather than capturing an image using a two-dimensional pixel matrix, the SPC employs a single photodetector in conjunction with a spatial light modulator (SLM), which sequentially measures the integrated radiation from specific portions of the observed scene. By acquiring a series of measurements using predefined spatial masks on the SLM, it is possible to reconstruct mathematically the image [26]. Sampling with orthogonal patterns-such as Hadamard matrices-enables image recovery via inverse linear transformations, thereby eliminating the need for pixelated sensor arrays [27]. In the context of carbon dioxide (CO_2) detection, SPCs can be configured to register radiation at wavelengths corresponding to key molecular absorption bands-namely, approximately 4.3 μm (asymmetric stretching vibration, $\nu 3$) and 15 μm (bending vibration, $\nu 2$). This capability facilitates remote, passive observation of the spatial distribution of CO_2 in the atmosphere by analyzing radiation from background sources whose spectral signatures are partially attenuated due to absorption by CO_2. Since the entire image acquisition process relies on a single detector element, the system design is simplified, calibration procedures are more straightforward, and issues related to pixel-to-pixel sensitivity variation are effectively eliminated.

A notable advantage of SPC imaging is its inherently high signal-to-noise ratio (SNR) [28]. This benefit stems from the fact that the total amount of radiation collected by the single detector in an SPC is substantially greater than that received by an individual pixel in a conventional array detector. Moreover, SPC architectures are compatible with advanced computational techniques that reduce the number of measurements required for accurate image reconstruction. One prominent example is compressed sensing (CS), which enables the recovery of high-quality images from a number of measurements significantly lower than the total number of pixels in the target image [29].

Recent developments have also focused on image reconstruction methods based on artificial intelligence, including convolutional neural networks (CNNs). These approaches enable the recovery of images from a reduced number of measurements, as well as their interpolation to higher spatial resolution [30, 31]. The application of such techniques holds practical significance in measurement systems-for instance, in the development of ultra-high-speed cameras [32] or economical imaging systems in spectral ranges for which array detectors are expensive. It should be noted, however, that SPC imaging technology exhibits several inherent limitations-the most critical being the time required for sequential sampling and the limited availability of suitable spatial light modulators (SLMs) operating in the MWIR and LWIR spectral ranges.

Ongoing research efforts are focused on the development of more efficient modulators, including concepts based on multilayer structures and metamaterials, such as hybrid plasmonic absorption modulators [33]. At present, however, mature and commercially viable solutions in this area remain unavailable. Despite these challenges, the SPC concept continues to offer a promising approach for the realization of compact infrared imaging systems. Such systems may find applications in atmospheric research, particularly in remote sensing and imaging of CO_2, by employing low-cost single-pixel detectors and mechanical spatial light modulators based on rotating patterned disks.

In this paper we present the quantitative protocol to measure carbone-dioxide concentration with uncertainty analysis. In addition, the absorption cross-section of CO_2 was experimentally confirm presenting the fidelity of our approach. We use the low-cost photographic-film SLM highly transparent for MWIR range. We use low-resolution cyclic measurement masks based on the Hadamard matrix and the interpolation up-sampling. Entire system is low-cost, efficient and can be easily implemented for practical quantitative applications.

2. Image reconstruction by a Single Pixel Camera

The multiband Single-Pixel Camera (SPC) system consists of rotating Hadamard-pattern Spatial Light Modulator (SLM) with an aperture size of 31 × 29 pixels. The SLM was made of photographic film and is driven by a DC motor reaching a speed up to 30 RPS (rotations per second). The synchronization of the disc rotation is determined by a marker in the form of a narrow gap placed on the edge of the SLM. In this way, beginning and end of the disc rotation are clearly visible on the recorded signal. The system setup with two lenses is shown in Figure 2.

Lens no. 1 allows to project and find focus of an object exactly at the modulator aperture. Lens no. 2 collects the signal from the modulator aperture and focuses it directly to the detector. The proposed system enables imaging in various spectral ranges from VIS to LWIR spectral range, simple by replacing detector. In order to reconstruct the images in this SPC, the Hadamard matrix $\mathbf{H}_{n\times n}$ with −1; +1 elements and the corresponding transformation matrix $\mathbf{S}(n-1) \times (n-1)$ called the Hadamard mask are generated. The transformation matrix $\mathbf{S}(n-1) \times (n-1)$ can be obtained from the Hadamard one just by eliminating the first row and column and changing the value of elements from −1; +1 to 1; 0 [34]. For $n = 4$, the mentioned matrixes take the forms:

$$\mathbf{H}_{4\times4} = \begin{bmatrix} 1 & 1 & 1 & 1 \\ 1 & -1 & 1 & -1 \\ 1 & 1 & -1 & -1 \\ 1 & -1 & -1 & 1 \end{bmatrix}, \quad \mathbf{S}_{3\times3} = \begin{bmatrix} 1 & 0 & 1 \\ 0 & 1 & 1 \\ 1 & 1 & 0 \end{bmatrix}. \tag{1}$$

The Hadamard $\mathbf{H}_{n\times n}$ and transformation $\mathbf{S}(n-1) \times (n-1)$ matrixes are generated using twin-primes algorithm that in addition allows to get cyclic Hadamard matrix [34]. In consequence the overlapped set of Hadamard patterns (apertures) can be easily arranged on the rotating SLM disk as shown in Figure 3. In the presented research the resolution of the images was established at 31 × 29 = 899 pixels.

The rotating SLM acts as the electro-mechanical system performing the Hadamard transform, that allows to obtain the Hadamard spectrum **HADSPEC**.

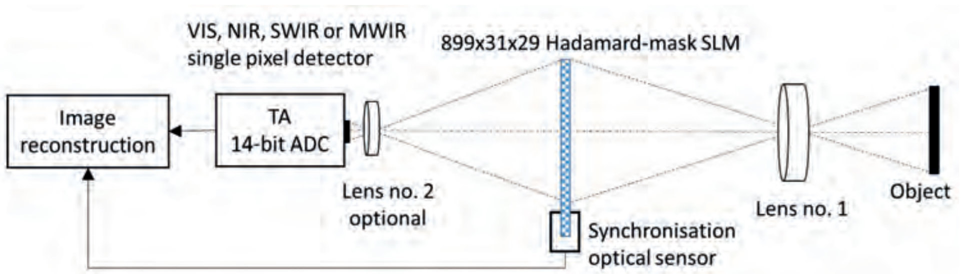

Fig. 2. A concept of multiband SPC
Rys. 2. Koncepcja obrazowania multispektralnego kamerą jednopikselową

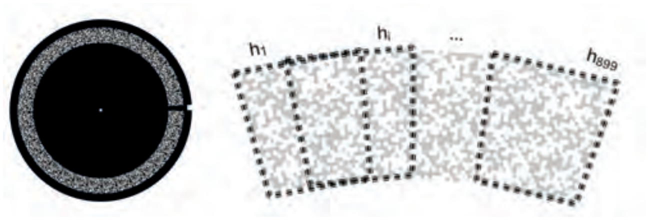

Fig. 3. SLM and overlapped Hadamard apertures

Rys. 3. Modulator SLM i nakładające się otwory Hadamarda

$$\mathbf{HADSPEC}_{899\times1} = \mathbf{S}_{899\times899} \times \mathbf{IM}_{899\times1}. \quad (2)$$

where $\mathbf{S}_{899\times899}$ is the transformation matrix, and $\mathbf{IM}_{899\times1}$ denotes a 31 × 29 pixel image reshaped to the 899 × 1 vector.

In practice, the image coding realised by the SLM is an integration of the image intensities corresponding to 899 patterns (apertures) with openings distributed according the transformation matrixes. Each aperture of the size 31 × 29 is created from each row of the transformation matrix $\mathbf{S}_{899\times899}$.

$$\mathbf{HADSPEC}(k) = \mathrm{A}\sum_{i,j=0}^{31,29}\mathbf{IM}(i,j)s_k(i,j) \quad (3)$$

where k is the index of k-th sample of the Hadamard spectrum, $k = 1...899$, s_k denotes the k-th row of the transformation matrix $\mathbf{S}_{899\times899}$, A is the apparatus constant.

Equations (2) and (3) form fully determined set of linear equation with 899 image's pixels that are unknowns. Due to the orthogonal feature of the Hadamard matrix and its cyclic character, the reconstruction of an image **recIM** can be easily carried out using the transposed matrix $\mathbf{S}^{\mathrm{T}}$.

$$\mathbf{recIM}_{899\times1} = \mathbf{S}^{\mathrm{T}}_{899\times899} \times \mathbf{HADSPEC}_{899\times1}. \quad (4)$$

3. Theoretical analysis

3.1. Estimation of absorption cross-section

According to the Beer-Lambert law and assuming a constant value of the extinction coefficient μ_λ, the spectral transmission of IR radiation through a gas takes the form:

$$\tau_\lambda = e^{-\mu_\lambda x} \quad (5)$$

where x is an optical path or the distance over which the gas attenuates IR radiation with a wavelength of λ.

By introducing the absorption cross section parameter α_λ [35], the effect of gas concentration C on the radiation attenuation due to absorption and scattering can be considered.

$$\mu_\lambda = \alpha_\lambda C = \alpha_\lambda \frac{N_{\mathrm{CO_2}}}{V} \quad (6)$$

where $N_{\mathrm{CO_2}}$ denotes the number of CO_2 molecules in volume V.

Considering the mixture of ideal gases, each gas can be analysed using the partial pressure p_{par}. For example for CO_2 in the atmosphere, using the relation $p_{\mathrm{par}} \cdot V = N_{\mathrm{CO_2}} \cdot k \cdot T$, we can rewrite equation (6) as:

$$\tau_\lambda = e^{-\alpha_\lambda\left(\frac{\gamma_{\mathrm{CO_2}} p}{kT}\right)x} \quad (7)$$

where $\gamma_{\mathrm{CO_2}}$ is the mass concentration of CO_2 in the atmosphere, e.g. 500 ppm = 0.05 % = 0.0005 for CO_2 in an open-air and non-industrial environment, p denotes the total pressure of the gas mixture, T is the absolute temperature, and the Boltzmann constant $k = 1.38 \times 10^{-23}$ J/K.

An important quantity of this simple model, which is not easily found in the literature for different gases, is the absorption cross-section area α_λ. The absorption cross-section refers to the probability of a photon interacting with a molecule. It can be calculated as the ratio of the extinction coefficient μ_λ to the concentration C, and appears in units of area, i.e. m². The absorption cross-section depends mainly on the type of gas, the photon wavelength, temperature, and pressure. As an example, let us assume T = 300 K, pressure p = 101,325 Pa, CO_2 concentration = 0.00032, and the absorption optical length L_{opt} = 100 m. The transmission coefficient for λ = 4.3 μm equals τ_λ = 0.098 [36]. This yields the absorption cross-section $\alpha_\lambda = 9.98 \times 10^{-18}$ cm².

3.2. Spectral characteristics of an IR acquisition system

The measurement system presented in this research consists of a single-detector MWIR (3–5 µm) head, a narrow-band pass filter for a given gas (CO_2 – 4.266 µm, FWHM = 150 nm, ϕ25 × 0.1 mm), SLM, and a black-body, all with wavelength-dependent characteristics. The output signal of the system S_{cam} can be presented as:

$$S_{\mathrm{cam}} = A_{\mathrm{app}}\int_{\lambda_{\min}}^{\lambda_{\max}} \tau_\lambda(\gamma_{CO_2}, L_{\mathrm{opt}})\tau_{\mathrm{filter}}\tau_{\mathrm{SLM}}R_{\mathrm{det}} \times F_{\mathrm{BB-det}}M_{\mathrm{BB}}A_{\mathrm{det}}d\lambda \quad (8)$$

where: A_{app} – apparatus constant, τ_{filter} – spectral characteristic of the filter, τ_{SLM} – spectral characteristic of the SLM, R_{det} – spectral sensitivity of the detector, $F_{\mathrm{BB-det}}$ – shape factor of the detector, optics, and the black-body (typically 0.2 for a lens with $F_{\#} = 1$), M_{BB} – spectral emission power (exitance) of the black-body, and A_{det} – area of the detector.

The spectral range of the analysis depends on the detector wavelength-dependent characteristic (MWIR 3–5 µm in this research) and the gas considered that has an impact on the IR narrow-band filter selection. Simplifying the problem by assuming that some quantities are wavelength independent in the considered radiation band (3–5 µm), the normalised output signal of the IR system takes a form:

$$S_{\mathrm{norm\_cam}} = \int_{\lambda_{\min}}^{\lambda_{\max}} \tau_\lambda(\gamma_{CO_2}, L_{\mathrm{opt}})\tau_{\mathrm{filter}}r_{\mathrm{det}}d\lambda \quad (9)$$

where r_{det} is the overall camera sensitivity, typically $0.2R_\lambda$. The absorption cross-section area for chosen gas can be evaluated using non-linear regression for equation (9).

4. Experimental setup and measurement system

The SPC system for CO_2 gas detection and concentration measurement comprises an MWIR detector with optical area A = 1 mm × 1 mm and a viewing angle of $\phi_{\mathrm{imm}} \approx 36°$, provided by the immersion lens. The spectral range of the detector is 2.7–5.2 µm, which was fabricated as an active heterostructure using the epitaxial deposition of HgCdTe [A1]. The SPC is equipped with an SLM with Hadamard masks. In order to measure the concentration of CO_2, a plastic tube 28 cm long was placed between the black-body and the detector. The labora-

Table 1. Measurement of output signal from single MWIR detector, without SLM
Tabela 1. Pomiar sygnału wyjściowego z pojedynczego detektora MWIR, bez SLM

CO_2, ppm	1,000	4,500	10,750	17,800	22,800	28,300
U, mV	23.4	–47.3	–92.3	–114	–123	–130

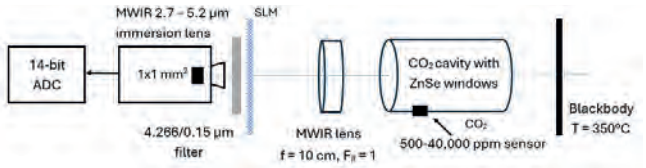

Fig. 4. Single-pixel IR camera for CO_2 gas detection and concentration measurement
Rys. 4. Jednopikselowa kamera termowizyjna do detekcji i pomiaru stężenia CO_2

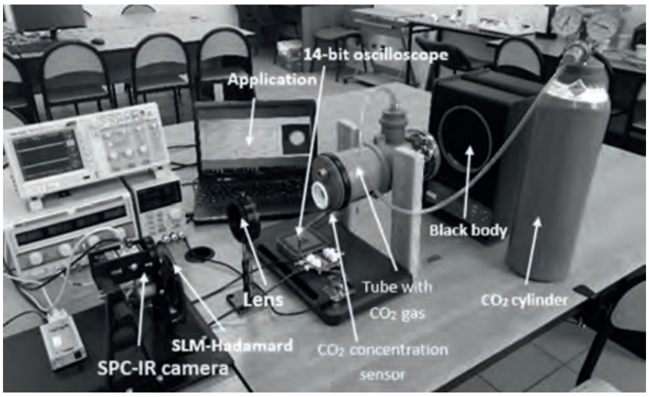

Fig. 5. Station for measuring CO_2 concentration using an SPC-IR camera
Rys. 5. Stanowisko do pomiaru stężenia CO_2 jednopikselową kamerą termowizyjną

tory setup is equipped with a precise gas concentration sensor (operating on the photoacoustic principle) located inside the tube at its bottom. Such an experimental rig allows for measuring the concentration in the range 500–40,000 ppm with an accuracy of ±50 ppm [A2]. To ensure stable gas measurement conditions, the tube was tightly closed using IR-transparent windows. On the black-body side, the tube was covered with transparent foil, while the front part of the tube was closed using a ZnSe window. The schematic diagram and a photo of the measurement system are presented in Figures 4 and 5.

4.1. Single-point measurement

In order to verify the quantitative measurement of gas concentration, the first experiment was carried out without SLM as shown in Figure 6. The radiation passes the gas in the tube and then is focused by the MWIR optics on a single detector. The output signal in digitalised by 14-bit oscilloscope.

The obtained results gathered in Table 1 allow us to present the change of the output signal vs. concentration measured by the photo-acoustic precise sensor. The shape of this characteristic agrees with the theory and it follows the exponentials relation between the output voltage and CO_2 concentration as shown in Figure 7– equation (10).

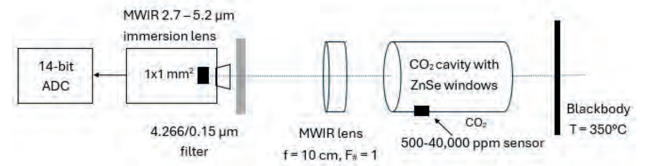

Fig. 6. Measurement setup for single MWIR detector, without SLM
Rys. 6. Układ pomiarowy pojedynczego detektora MWIR bez modulatora SLM

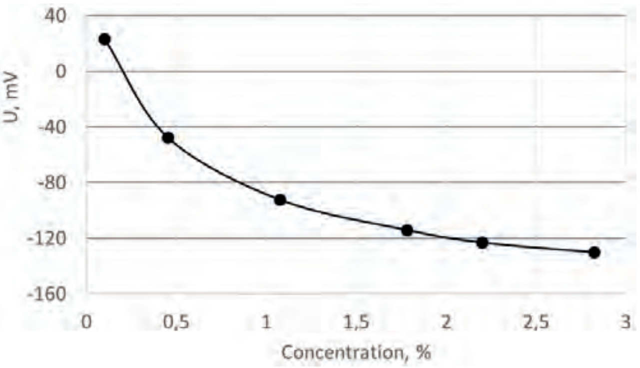

Fig. 7. Approximation of measured signal of the IR detector vs. concentration of CO_2 performed according to the setup in fig. 6
Rys. 7. Przybliżenie sygnału zmierzonego przez pojedynczy detektor w funkcji stężenia CO_2 wykonane zgodnie z konfiguracją przedstawioną na rys. 6

$$U = a_1 + a_2 \cdot e^{a_3 C} \tag{10}$$

where concentration C is expressed in ppm, and $a_1 = -128.16$ mV, $a_2 = 175.13$ mV, and $a_3 = 157.86$.

After normalization, we can present the transmission coefficient $\tau(C)$ as a function of concentration C:

$$\tau(C) = \frac{U - a_1}{a_2} = e^{-a_3 C} \tag{11}$$

At last, assuming $L = 0.28$ m, $T = 300$ K and $p = 100{,}300$ Pa, the absorption cross section can be evaluated using

$$\alpha_\lambda = \frac{ckT}{pL} = 2.33 \times 10^{-19}\,\mathrm{cm}^2 \tag{12}$$

The last result agrees with the appropriate data for CO_2 that can be found in literature [A3].

4.2. Signal processing and image reconstruction

In order to analyse the signal obtained from a single detector, a dedicated application was written in C# language (as a Windows Forms application in the *.NET Framework*). The main window of this application is shown in Figure 8. First, the application connects to the 14-bit oscilloscope (Analog Discovery 3), which is a multifunctional computer adapter with the USB-C interface [A4]. This device works as a 2-channel oscilloscope. The first channel acquires the signal from the detector while the second channel records the signal from the slot optocoupler. It ensures synchronization of image acquisition with the rotation of the SLM modulator. In order to reconstruct the image of the observed scene, it is necessary to select the appropriate part of the signal from the beginning to the end of the modulation. This can be done by using opaque separators between the start and end in the modulator ring. This is visualized on the first channel signal as negative peaks, as seen in the top graph in Figure 8.

Alternatively, the synchronization signal from the slit optocoupler can be used for indicating a full rotation of the SLM modulator as presented in the bottom graph in Figure 8.

The block diagram in Figure 9 shows the overall signal processing starting with the detector and ending with the quantitative CO_2 concentration measurement in the atmosphere. The SLM

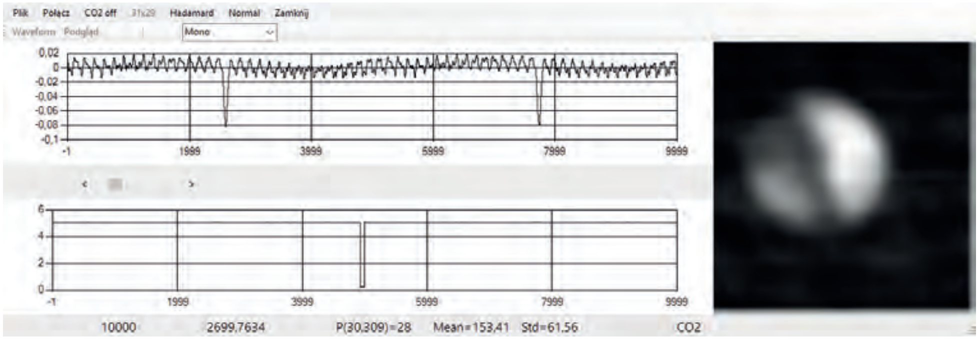

Fig. 8. An application for image reconstruction from a single-detector. Signal at the top – from a single detector. Signal at the bottom – from the slot optocoupler
Rys. 8. Aplikacja do rekonstrukcji obrazu z pojedynczego detektora. Sygnał u góry – z pojedynczego detektora. Sygnał na dole – z transoptora szczelinowego

modulator is made from photographic film on which Hadamard masks of 31 × 29 pixels are exposed. The presented system uses an infrared lens placed between the observed object and the modulator. The purpose of this lens is to precisely project the scene's infrared radiation onto the part of the SLM modulator where the Hadamard mask is located. The signal generated by the single detector is then amplified by a transimpedance amplifier. The examples visualizing the CO_2 outflow at different volumetric velocities are presented in Figure 10. It is worth noting that the SPC was operated with the SLM rotating at approximately 30 RPS, which allowed for real-time flow display.

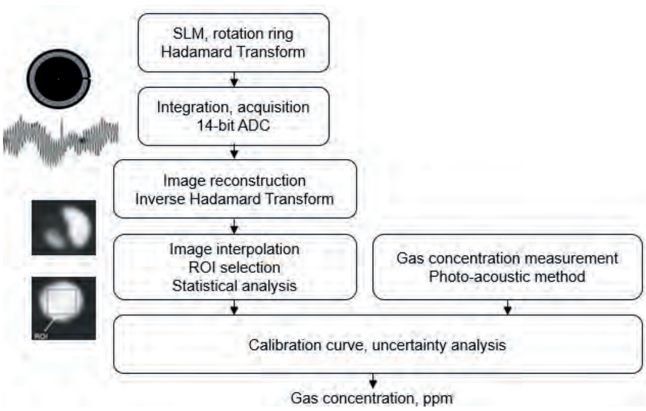

Fig. 9. Block diagram of an application for reading and reconstruction signal from a single-detector
Rys. 9. Schemat blokowy aplikacji umożliwiającej odczyt i rekonstrukcję sygnału z pojedynczego detektora

5. Experimental results and CO_2 concentration measurement

The measurement of CO_2 concentration was performed using the setup presented in Figures 4 and 5. The images were reconstructed using the Hadamard masks. The developed single-pixel camera was placed in front of a tube in which CO_2 was mixed with air to obtain different concentrations. At the back of the measurement system there was a black body emitting infrared radiation at a temperature of 350 °C. This radiation, passing through the gas mixture in the tube, was then focused on the SLM and finally on the detector. The examples of reconstructed images for different CO_2 concentrations are presented in Figure 11a,b,c. At first, the reference image without additional CO_2 inside the tube was recorded – Figure 11a. Then, the signals were acquired and images were reconstructed for 10 different concentrations, ranging from about 1,000 ppm to 32,500 ppm. For each concentration, measured by the CO_2 photo-acoustic sensor, five measurements were taken every five seconds. The output signal used for estimation of CO_2 concentration was measured for pixels within a region of interest (ROI) area as indicated in Figure 11a. The ROI contains approximately 14,500 pixels. It should be noted that the original images with a resolution of 31 × 29 pixels were interpolated ten times to visualize them on the screen. Table 2 shows the measured values of statistical parameters for the considered ROI in the reconstructed images. As expected, we can observe that the image intensity value decreases with increasing CO_2 content inside the tube.

5.1. Uncertainty analysis

5.1.1. Type A uncertainty

The measurements for uncertainty analysis were performed with a blackbody temperature of 350 °C. Ten different CO_2 concentrations were measured in the range from 975 ppm (atmospheric) to 32,503 ppm (Table 2), which was the highest available for reliable measurement with the reference sensor Sensirion SCD40-D-R1. For each concentration, measurements were taken using both the developed apparatus and the reference sensor. The aim of this analysis was to determine the value of expanded uncertainty, which involves both type A and type B uncertainty, as described below. The developed system enables us to obtain the signal for each pixel in the reconstructed image. This signal s_{DL} is expressed in DL units (Digital Level) in the range 0–255 and is calculated as the mean value of approximately $N = 14{,}500$ pixels. Simultaneously, the concentration C is measured in the tube partially filled with CO_2. The S_{DL} signal correlates nonlinearly and inversely with the concentration C, as seen in Table 2. At first, the fitting of the SPC output signal S_{DL} and concentration C was performed and is expressed by:

$$S_{DL} = a_1 + a_2 \cdot e^{-a_3 C} \qquad (13)$$

where: $a_1 = 50.38$, $a_2 = 209.47$, $a_3 = 169.44$.

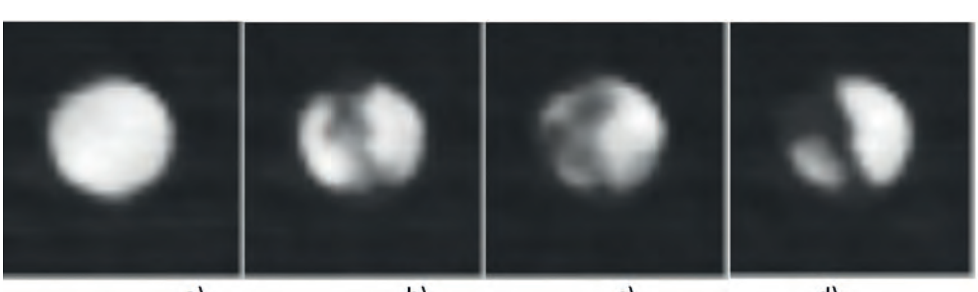

Fig. 10. a) No-flow, b) 5 l/min, c) 10 l/min, d) 15 l/min
Rys. 10 a) Brak przepływu gazu, b) 5 l/min, c) 10 l/min, d) 15 l/min

Table 2. Experimental results of CO_2 concentration while imaging (DL – digital level)
Tabela 2. Wyniki eksperymentalne dotyczące koncentracji CO_2 podczas obrazowania (DL – poziom cyfrowy)

CO_2 concentration (ppm)	Mean value DL	Standard deviation DL
976	227.57	15.43
1,806.8	208.51	21.67
3,327.6	167.41	15.13
5,677.6	123.98	9.50
8,726.4	104.04	7.24
11,939	82.77	6.28
18,522.2	64.46	5.54
24,806.6	53.25	4.36
28,002.6	50.77	3.59
32,503.2	46.90	3.22

The inverse function of (13) can represent a calibration curve:

$$C = -\frac{1}{a_3}\ln\left(\frac{S_{\mathrm{DL}} - a_1}{a_2}\right) \tag{14}$$

In order to calculate type u_{A} uncertainty of the concentration C, the derivative $\frac{dC}{ds_{DL}}$ has to be determined:

$$\frac{dC}{dS_{\mathrm{DL}}} = -\frac{1}{a_3(S_{\mathrm{DL}} - a_1)} \tag{15}$$

Finally, we can estimate type u_{A} uncertainty for the concentration C as:

$$u_{\mathrm{A}} = \left|\frac{dC}{dS_{\mathrm{DL}}}\right| u_{\mathrm{A-DL}} = \frac{1}{a_3(S_{\mathrm{DL}} - a_1)} u_{\mathrm{A-DL}} \tag{16}$$

where uncertainty $u_{\mathrm{A-DL}}$ is calculated for the averaged measurements for $N = 14{,}500$ pixels and takes a form [A5]:

$$u_{\mathrm{A-DL}} = \sqrt{\frac{\sum_{i=1}^{N}\left(S_{\mathrm{DL}i} - \overline{S_{\mathrm{DL}}}\right)^2}{N(N-1)}} \tag{17}$$

5.1.2. Type B uncertainty

Type B uncertainty refers to the uncertainty that is derived from sources other than statistical analysis of repeated measurements. It is often based on known or assumed information, such as specifications, manufacturer's tolerances, calibration data, or expert judgment. Type B uncertainties can arise from systematic errors, environmental factors, or instrument calibration, and they are typically quantified by evaluating the accuracy of the measuring equipment, the conditions under which measurements are taken, and any other relevant information. Unlike Type A uncertainty, which is calculated from measurement data, Type B uncertainty needs to be estimated from external sources. In the case of the performed experiment, the Type B uncertainty u_{B} can be associated with the measurement accuracy of the reference devices. In this research, two reference measurement elements were taken into account: a 14-bit A/D acquisition system allowing the conversion of the radiation signal into reconstructed images, and a blackbody used as background illumination of an absorbing gas. It was assumed that the maximum error of the measured signal generated by the acquisition system with 14-bit resolution is ±3 bits. Taking into account the range of the output data corresponding to the pixel representation in an image ($pix_{range} = 0$–255), the maximum error is estimated as:

$$U_{\mathrm{B1}} = \frac{\Delta_{A/D_{\max}}}{\sqrt{3}} = \frac{pix_{range}}{\sqrt{3}\cdot 2^{11}} \tag{18}$$

According to the datasheet [A6], the blackbody stability is equal to ±0.4 °C. In order to determine the influence of blackbody temperature changes on the signal changes (in DL), the authors measured the relationship between these parameters, given by the formula (19) obtained through curve fitting.

$$S_{\mathrm{DL}} = c_1 \cdot T^{C_2} \tag{19}$$

where $c_1 = 2.697 \times 10^{-6}/(°\mathrm{C})^{-2.9477}$, $c_2 = 2.9477$.

It is estimated that a blackbody temperature change of 0.4 °C at 350 °C causes a digital level (DL) change of 0.82 °C. As a result, the maximum error caused by the blackbody, expressed in DL units, is $\Delta_{\mathrm{BBmax}} = 0.33$.

$$u_{\mathrm{B2\text{-}DL}} = \left|\frac{dC}{dS_{\mathrm{DL}}}\right|\frac{\Delta_{\mathrm{BB\,max}}}{\sqrt{3}} \tag{20}$$

5.1.3. Expanded uncertainty

The combined standard uncertainty u_{C} is the combination of type A uncertainty (from the standard deviation of the measurements) and type B uncertainty (from the references of used measurement devices). Since these uncertainties are independent, we combine them using the square root of the sum of squares, as shown in Equation (21). Finally, we calculate the expanded uncertainty U_{exp} by multiplying the total uncertainty by the coverage factor $k = 2$ for a 95 % confidence level.

$$U = k\sqrt{u_{\mathrm{A}}^2 + u_{\mathrm{B}_1}^2 + u_{\mathrm{B}_2}^2} \tag{21}$$

It can be observed that all uncertainties increase with concentration. For the lowest concentration, the dominant uncertainty component is type A. For the highest concentration, the uncertainty arises due to the apparatus used, mainly oscilloscope and blackbody accuracy and stability. Overall, the expanded uncerta-

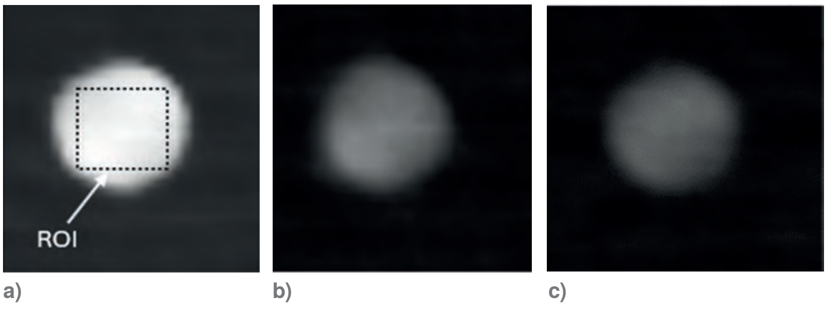

Fig. 11. IR image of a black body recorded by an SPC camera, viewed through a tube with CO_2 gas at three different concentrations: (a) 1000 ppm, (b) 5673 ppm, and (c) 11,678 ppm
Rys. 11. Obraz w podczerwieni ciała czarnego zarejestrowany przez kamerę jednopikselową, oglądany przez tubę wypełnioną gazem CO_2 o trzech różnych stężeniach: (a) 1000 ppm, (b) 5673 ppm, (c) 11 678 ppm

inty value does not exceed 6 % of measured concentration value in all cases, what is acceptable for many practical applications.

6. Discussion

The presented SPC system for CO_2 detection and concentration measurement exhibits both limitations and advantages, arising from the implemented technological solutions and the fundamental principles of its operation. A primary limitation is the use of a rotational SLM fabricated on a photographic substrate. The film bearing the encoded pattern is characterized by low mechanical stability, manifested in its susceptibility to deformations, vibrations, and surface irregularities. These defects result in unstable modulation patterns of the infrared radiation. Uncontrolled pattern shifts may also occur due to friction and desynchronization between the physical SLM aperture and the mathematical pattern. Both phenomena can lead to image reconstruction errors. Moreover, the limited precision of the pattern on the foil and the off-center placement adversely affect the geometric accuracy of the modulator, which significantly affects the efficiency of image coding and reconstruction. The spatial resolution of the SLM, currently 31 × 29 pixels, is insufficient for more advanced applications, such as imaging dynamic scenes with a high level of detail. Increasing the resolution has two main consequences: the resolution is determined by the occurrence of adjacent twin prime numbers p and q, where $q = p + 2$, and inevitably leads to an increase in the diameter of the encoding disk due to the extension of the coding mask.

An alternative approach would involve replacing the rotational SLM with a digital light modulator based on digital micromirror device (DMD) technology capable of modulating MWIR radiation [37], or implementing a modulator based on graphene oxide technology [38]. These solutions could provide a higher number of coding patterns in a shorter time, along with increased spatial resolution. However, at the current stage, SLM solutions for the MWIR range remain underdeveloped. The application of DMDs for MWIR is challenging due to technology primarily designed for visible light, while matrix-based solutions employing graphene have not yet progressed beyond research and experimental phases. The second limitation arises from the use of a fast HgCdTe detector for spatio-temporal measurement. To reconstruct a single image, it is necessary to perform a series of rapid measurements, which excludes the use of inexpensive bolometric detectors characterized by significant thermal inertia.

A further key aspect concerns noise reduction and improving the signal-to-noise ratio (SNR). The currently used method of averaging signals within the region of interest (ROI) partially reduces noise; however, further improvement in measurement precision may be achieved by employing advanced signal processing techniques. The measurement uncertainty of both type A and type B reaches its minimum relative to the gas concentration in the range of 3,000–12,000 ppm. For higher gas concentration, the uncertainty increases due to the lower amount of radiation reaching the detector. For low gas concentration, close to atmospheric levels, the SNR is also lower due to the small difference between attenuated and unattenuated readouts under a constant detector noise level. In addition, the relative error of carbon dioxide measurement (U_{exp}/C) tends to increase at low CO_2 concentrations, as shown in Table 3.

7. Conclusions

The conducted research has demonstrated that the application of SPC technology with a convolutional neural network for detecting and measuring CO_2 concentration in the MWIR range represents an interesting alternative to conventional array-based methods. The aim of using CNN was to increase the image resolution to 80 × 80 pixels. A single aperture in the SLM modulator has only 31 × 29 pixels. The CNN architecture was presented in the earlier article [39]. The system enabled the acquisition of spatial gas distribution images using Hadamard masks with a rotating SLM, confirming the potential of this technology for gas imaging. The measurement accuracy was determined by an expanded uncertainty of up to 6 %, which is comparable to or slightly worse than other non-dispersive measurement methods [13]. At the current stage, the achieved uncertainty value limits the system's applicability to preliminary environmental monitoring, gas leak detection, or air quality analysis, where a moderate error level is acceptable. The system's limitations stem, among others, from the low resolution of the mechanical spatial light modulator and the precision of aligning the actual SLM mask to the mathematical pattern matrix.

Many of the shortcomings identified in the discussion suggest the potential for improving the system's quality and resolution through the use of digitally controlled SLMs, such as DMD arrays, or graphene-based modulators. The use of machine learning algorithms for image reconstruction allowed for a reduction in the number of samples while simultaneously increasing image resolution, serving as a significant alternative to compressed

Table 3. Uncertainty determination for different gas concentrations
Tabela 3. Analiza niepewności błędu dla różnych stężeń gazu

No.	Concentration (ppm)	U_A (ppm)	U_{B1} (ppm)	U_{B2} (ppm)	U_{exp} (ppm)	U_{exp}/C (%)
1	976	4.26	2.40	3.63	12.18	1.24
2	1,806.8	6.89	2.76	4.18	17.03	0.94
3	3,327.6	6.22	3.57	5.41	17.97	0.54
4	5,677.6	5.82	5.32	8.06	22.54	0.40
5	8,726.4	7.43	8.92	13.51	35.62	0.41
6	11,939.0	11.11	15.37	23.28	60.05	0.50
7	18,522.2	29.90	46.90	71.02	180.41	0.97
8	24,806.6	68.25	136.03	205.97	512.19	2.06
9	28,002.6	96.58	233.79	353.99	870.15	3.11
10	32,503.2	185.71	501.20	758.88	1,856.43	5.71

sensing while maintaining short processing times during image reconstruction, representing a key step towards more efficient measurement methods.

In summary, the presented research highlights the potential development of SPC technology towards compact, cost-effective single-detector infrared imaging systems that may find applications in atmospheric monitoring, though further work is needed to improve measurement precision.

References

1. Bachhav R., Bachhav M., Sonawane V., Sonawane G., *A brief review on different chromatographic techniques*, "Open Access Journal of Pharmaceutical Research", Vol. 8, No. 1, 2024, DOI: 10.23880/oajpr-16000294.
2. Saeed I.M., Mazari S.A., Alaba P., Ali B.S., Jan B.M., Basirun W.J., Sani Y.M., Nizzamuddin S., Mubarak N.M., *A review of gas chromatographic techniques for identification of aqueous amine degradation products in carbonated environments*, "Environmental Science and Pollution Research", Vol. 28, No. 6, 2021, 6324–6348, DOI: 10.1007/s11356-020-11753-5.
3. Duarte A.R.C., Anderson L.E., Duarte C.M.M., Kazarian S.G., *A comparison between gravimetric and in situ spectroscopic methods to measure the sorption of CO_2 in a biocompatible polymer*, "The Journal of Supercritical Fluids", Vol. 36, No. 2, 2005, 160–165, DOI: 10.1016/j.supflu.2005.04.003.
4. Baranwal J., Barse B., Gatto G., Broncova G., Kumar A., *Electrochemical sensors and their applications: A review*, "Chemosensors", Vol. 10, No. 9, 2022, DOI: 10.3390/chemosensors10090363.
5. Tanjeem N., Kawazoe T., Yatsui T., *CO_2 phonon mode renormalization using phonon-assisted energy up-conversion*, "Scientific Reports", Vol. 3, No. 1, 2013, DOI: 10.1038/srep03341.
6. Chabbi H., Dahoo P.R., Dubost H., Gauthier-Roy B., Vasserot A.-M., Abouaf-Marguin L., *Experimental analysis of $^{13}CO_2$ infrared stimulated emissions in solid argon*, "Low Temperature Physics", Vol. 26, No. 9, 2000, 719–726, DOI: 10.1063/1.1312399.
7. Wahab M.A., *Normal Modes of Molecular Vibrations*, [In:] Symmetry Representations of Molecular Vibrations, CHEMICAL, Vol. 126, 2022, 191–250, DOI: 10.1007/978-981-19-2802-4_4.
8. Kozák T., Bogaerts A., *Splitting of CO_2 by vibrational excitation in non-equilibrium plasmas: a reaction kinetics model*, "*Plasma Sources Science and Technology*", Vol. 23, No. 4, 2014, DOI: 10.1088/0963-0252/23/4/045004.
9. Wu X., Zhang L., Zhang S., Ye D., *Theory of dipole moment reconstruction by attosecond transient absorption spectroscopy*, "Physical Review A", Vol. 104, No. 6, 2021, DOI: 10.1103/PhysRevA.104.063121.
10. White D.W., Mastrapa R.M., Sandford S.A., *Laboratory spectra of CO_2 vibrational modes in planetary ice analogs*, "Icarus", Vol. 221, No. 2, 2012, 1032–1042, DOI: 10.1016/j.icarus.2012.10.024.
11. Xu F., *Photoresponsive supramolecular polymers*, [In:] "Photoactive Functional Soft Materials: Preparation, Properties, and Applications", 2019, 45–90, DOI: 10.1002/9783527816774.ch2.
12. Bogue R., *Detecting gases with light: a review of optical gas sensor technologies*, "Sensor Rewiev", Vol. 35, No. 2, 2015, 133–140, DOI: 10.1108/SR-09-2014-696.
13. Jha R.K., *Non-dispersive infrared gas sensing technology: A review*, "IEEE Sensors Journal", Vol. 22, No. 1, 2022, 6–15, DOI: 10.1109/JSEN.2021.3130034.
14. Tran D., Gorius N., Quilligan G.T., Gong Q., Kolasinski J.R., Purser T.C., Siguelnitzky A., Parker J.E., Wegel D.C., Glavin D.P., Gerakines P.A., Aslam S., Nehmetallah G., *Gas analyzer for monitoring H_2O and CO_2 partial pressures in space instrumentation*, "IEEE Sensors Journal", Vol. 22, No. 13, 2022, 12 576–12 587, DOI: 10.1109/JSEN.2022.3177079.
15. Wang G., Cui R., Di J., Wang Y., Wang J., Feng C., Chen Y., Wu H., Dong L., *Compact TDLAS sensor system for ppm-level CO detection in early electrical fires using a low-power laser diode and miniature multipass cell*, "IEEE Sensors Journal", Vol. 25, No. 10, 2025, 18 163–18 170, DOI: 10.1109/JSEN.2025.3543533.
16. Platt U., *Differential optical absorption spectroscopy, air monitoring by*, [In:] "Encyclopedia of Analytical Chemistry", 2006, DOI: 10.1002/9780470027318.a0706.
17. Haiming Z., *Experiment study of continuous emission monitoring system based on differential optical absorption spectroscopy*, [In:] 2008 International Workshop on Education Technology and Training & 2008 International Workshop on Geoscience and Remote Sensing, IEEE, 2008, 175–177, DOI: 10.1109/ETTandGRS.2008.29.
18. Chen K., Zhang B., Guo M., Chen Y., Deng H., Yang B., Liu S., Ma F., Zhu F., Gong Z., Yu Q., *Photoacoustic trace gas detection of ethylene in high-concentration methane background based on dual light sources and fiber-optic microphone*, "Sensors and Actuators, B: Chemical", Vol. 310, 2020, DOI: 10.1016/j.snb.2020.127825.
19. Zhao X., Chen K., Guo M., Li C., Li C., Zhang G., Gong Z., Zhou Z., Peng W., *Ultra-high sensitive multipass absorption enhanced fiber-optic photoacoustic gas analyzer*, "IEEE Transactions on Instrumentation and Measurement", Vol. 72, 2022, DOI: 10.1109/TIM.2022.3188043.
20. Selvaraj R., Vasa N.J., Shiva Nagendra S.M., *Off-resonant broadband photoacoustic spectroscopy for online monitoring of biogas concentration with a wide dynamic range*, [In:] Conference on Lasers and Electro-Optics (CLEO), 2019, DOI: 10.1364/CLEO_AT.2019.JW2A.20.
21. Zhang H., Bi S., Zhao J., Zhao Y., Qin L., Shi J., Fu Y., Wang Z., *Dual-gas intra-cavity QEPAS sensor based on frequency division multiplexing using two acoustic micro-resonators*, "Journal of Lightwave Technology", Vol. 42, No. 14, 2024, 5033–5040, DOI: 10.1109/JLT.2024.3379488.
22. Hu P., Pan S., Cheng C., Qi H., Liu S., Chen N., *Measurement of carbon dioxide by near-infrared cavity ring-down spectroscopy*, [In:] 2022 20th International Conference on Optical Communications and Networks (ICOCN), IEEE, 2022, DOI: 10.1109/ICOCN55511.2022.9900944.
23. Bai J., Niu Z., Bi K., Yang X., Huang Y., Fu Y., Wu M., Wang L., *Toward an advanced method for full-waveform hyperspectral LiDAR data processing*, "IEEE Transactions on Geoscience and Remote Sensing", Vol. 62, 2024, DOI: 10.1109/TGRS.2024.3382481.
24. Yue B., Yu S., Li M., Wei T., Yuan J., Zhang Z., Dong J., Jiang Y., Yang Y., Gao Z., Xia H., *Local-scale horizontal CO_2 flux estimation incorporating differential absorption lidar and coherent doppler wind lidar*, "Remote Sensing", Vol. 14, No. 20, 2022, DOI: 10.3390/rs14205150.
25. Yu S., Zhang Z., Xia H., Dou X., Wu T., Hu Y., Li M., Shangguan M., Wei T., Zhao L., Wang L., Jiang P., Zhang C., You L., Tao L., Qiu J., *Photon-counting distributed free--space spectroscopy*, "Light: Science & Applications", Vol. 10, No. 1, 2021, DOI: 10.1038/s41377-021-00650-2.
26. Osorio Quero C.A., Durini D., Rangel-Magdaleno J., Martinez-Carranza J., *Single-pixel imaging: An overview of different methods to be used for 3D space reconstruction in harsh environments*, "Review of Scientific Instruments", Vol. 92, No. 11, 2021, DOI: 10.1063/5.0050358.
27. Hahamovich E., Monin S., Hazan Y., Rosenthal A., *Single pixel imaging at megahertz switching rates via cyclic Hada-*

mard masks, "Nature Communications", Vol. 12, No. 1, 2021, DOI: 10.1038/s41467-021-24850-x.
28. Liu Y., Gutierrez-Barragan F., Ingle A., Gupta M., Velten A., *Single-photon camera guided extreme dynamic range imaging*, [In:] 2022 IEEE/CVF Winter Conference on Applications of Computer Vision (WACV), IEEE, 2022, 41–51, DOI: 10.1109/WACV51458.2022.00012.
29. Candès E.J., Romberg J.K., Tao T., *Stable signal recovery from incomplete and inaccurate measurements*, "Communications on Pure and Applied Mathematics", Vol. 59, No. 8, 2006, 1207–1223, DOI: 10.1002/cpa.20124.
30. Szajewski K., Szajewska A., Urbaś S., Więcek B., *Review on infrared single-pixel imaging*, "Opto-Electronics Review", Vol. 33, No. 2, 2025, DOI: 10.24425/opelre.2025.154306.
31. Moodley C. Forbes A., *Super-resolved quantum ghost imaging*, "Scientific Reports", Vol. 12, No. 1, 2022, DOI: 10.1038/s41598-022-14648-2.
32. Liu Z., Li D., Yan P., Gong M., Xiao Q., *Single-pixel high--speed imaging through a multimode fiber*, [In:] 2022 Conference on Lasers and Electro-Optics (CLEO), 2022.
33. Soofi H., Bagheri S.K., Vahed H., *Design and modeling of graphene based electro-absorption modulator integrated with hybrid plasmonic waveguides*, [In:] 2024 32nd International Conference on Electrical Engineering (ICEE), 2024, DOI: 10.1109/ICEE63041.2024.10667917.
34. Harwit M., Sloane N.J., *Hadamard Transform Optics*, Academic Press INC, 1979, DOI: 10.1016/B978-0-12-330050-8.X5001-X.
35. McHale J.L., *Molecular spectroscopy*, Prentice Hall, 2017, DOI: 10.1201/9781315115214.
36. Gaussorgues G., *La thermographie infrarouge: principes, technologies, applications*, 4th ed., TEC & DOC, 2000.
37. Jin X.-P., Xiong A.-D., Wang X.-Q., Yao X.-R., Liu X.-F., Zhao Q., *Long-distance mid-wave infrared super-resolution compressive imaging*, "Optics and Laser Technology", Vol. 157, 2023, DOI: 10.1016/j.optlastec.2022.108740.
38. Ruan Z., Pei L., Wang J., Zheng J., Wang J., Li J., Ning T., Zhao Q., Xie Y., *All-optical graphene oxide modulator based on phase-shifted FBG*, "Journal of Lightwave Technology", Vol. 39, No. 17, 2021, 5516–5522, DOI: 10.1109/JLT.2021.3085350.
39. Urbaś S., Więcek S., *Application of a deep-learning neural network for image reconstruction from a single-pixel infrared camera*, "Opto-Electronics Review", Vol. 32, No. 1, 2024, DOI: 10.24425/opelre.2024.148877.

Other sources

A1. VIGO Photonics S.A., *Pvi-5 detector series*, [https://vigophotonics.com/app/uploads/2024/07/PVI-5-detector-series-datasheet.pdf].
A2. Sensirion AG, *SCD40 – compact & cost-effective photoacoustic NDIR CO_2 sensor*, [https://sensirion.com/media/documents/48C4B7FB/67FE0194/CD_DS_SCD4x_Datasheet_D1.pdf].
A3. NIST Chemistry WebBook, *Carbon dioxide*, [https://webbook.nist.gov/cgi/cbook.cgi?ID=C124389&Type=IR-SPEC&Index=0#IR-SPEC].
A4. Digilent co NI, *Analog discovery 3 reference manual*, [https://digilent.com/reference/test-and-measurement/analog-discovery-3/reference-manual].
A5. Joint Committee for Guides in Metrology, *Evaluation of measurement data – guide to the expression of uncertainty in measurement*, 2008, [https://ncc.nesdis.noaa.gov/documents/documentation/JCGM_100_2008_E.pdf].
A6. Fluke Corporation, *Fluke calibration 4180/4181 precision IR calibrators*, [www.fluke.com/pl-pl/produkt/przyrzady-do-kalibracji/kalibratory-temperatury/fluke-calibration-4180-4181].

Detekcja i pomiar stężenia gazu z wykorzystaniem jednopikselowej kamery termowizyjnej

Streszczenie: W artykule przedstawiono innowacyjną metodę detekcji i ilościowego pomiaru dwutlenku węgla (CO_2) z wykorzystaniem kamery jednopikselowej (SPC) działającej w zakresie podczerwieni średniofalowej (MWIR). Zamiast konwencjonalnej matrycy detektorów, system wykorzystuje pojedynczy fotodetektor HgCdTe sprzężony z obrotowym przestrzennym modulatorem światła (SLM) kodowanym cyklicznymi maskami Hadamarda. Rekonstrukcja obrazu jest realizowana matematycznie w oparciu o pomiary sekwencyjne, co umożliwia zarówno poprawę jakości obrazu, jak również interpolację przy ograniczonej liczbie próbek. Opracowany system pozwala na generowanie dwuwymiarowych obrazów rozkładu promieniowania podczerwonego osłabionego obecnością CO_2, umożliwiając zdalną ocenę jego stężenia. Eksperymenty laboratoryjne przeprowadzono z wykorzystaniem kontrolowanej komory gazowej i referencyjnego czujnika fotoakustycznego. Wyniki potwierdzają zdolność systemu do dokładnego pomiaru stężeń CO_2 w zakresie 1000–32 500 ppm, z błędem nieprzekraczającym 6 %. Proponowana technologia łączy niski koszt detektora z wysoką czułością i możliwościami obrazowania przestrzennego. Wykazuje ona obiecujący potencjał w zastosowaniach w monitoringu środowiska, wykrywaniu wycieków gazu oraz w kompaktowych systemach do analizy jakości powietrza i atmosfery.

Słowa kluczowe: jednopikselowa kamera termowizyjna, absorpcja CO2 MWIR, cykliczna macierz Hadamarda

Sebastian Urbaś, PhD Eng.

sebastian.urbas@dokt.p.lodz.pl
ORCID: 0000-0002-7699-5425

He received the PhD degree from Lodz University of Technology in 2026. The main areas of interest are embedded electronics, computer thermography, signal and image processing and development of IR systems, PLC and SCADA systems.

Robert Olbrycht, DSc PhD Eng.

robert.olbrycht@p.lodz.pl
ORCID: 0000-0001-9842-2815

He received the DSc degree from Lodz University of Technology in 2025. His research focuses on thermographic methods of optical gas imaging for detecting unwanted gas emissions. He is affiliated with the Institute of Electronics at Lodz University of Technology, where he conducts research on thermal imaging camera modelling, non destructive testing, and cultural heritage protection. His work includes the design and development of specialized thermal imaging systems for advanced applications. He is the co author of numerous scientific publications and books in the fields of thermography and infrared spectrometry.

Krzysztof Szajewski, MSc Eng.

krzysztof.szajewski@wat.edu.pl
ORCID: 0000-0002-8429-3976

He graduate of the Faculty of Cybernetics at the Military University of Technology. Since 2021, he has been employed at the Faculty of Cybernetics of the Military University of Technology. He also works at the Observation and Reconnaissance Systems Laboratory at the Air Force Institute of Technology. His interests focus on prototyping digital electronic devices, digital imaging, and digital signal processing.

Anna Szajewska, PhD Eng.

aszajewska@apoz.edu.pl
ORCID: 0000-0001-8370-6807

Assistant Professor at the Fire University in Warsaw, Faculty of Safety Engineering and Civil Protection. Research interests include external fire development, digital image processing, infrared imaging technology, and thermal imaging applications.

Prof. Bogusław Więcek, DSc PhD Eng.

boguslaw.wiecek@p.lodz.pl
ORCID: 0000-0002-5003-1687

He is the head of the Department of Electronic Circuits and Thermography at the Institute of Electronics of the Lodz University of Technology. He specializes in computer thermography and modelling of thermal problems in electronic systems. He is a member of the scientific committee of the international Conference on Quantitative Infrared Thermography (QIRT) and chairman of the Conference on Infrared Thermography and Thermometry organized periodically in Poland.